Aeroelastic flutter of Functionally Graded Beams reinforced with Hydrogen-Functionalized Graphene Nanoplatelets

ABSTRACT

This paper studies aeroelastic flutter behaviors of hydrogen-functionalized graphene nanoplatelet-reinforced composite (HFGRC) beams. Displacements of the beams are described based on the first-order shear deformation theory (FSDT). Material properties of the HFGRCs are predicted by the micromechanics models which have been modified by machine learning (ML) assistance. Combined with Ritz trial functions, Hamilton's principle is employed to derive the dynamic equations of the beams under supersonic airflow. The eigenvalue equation is derived and is numerically solved to get the flutter velocities. A detailed parametric study is conducted to investigate the effect of boundary conditions, GPL distribution pattern, temperature change, and hydrogenation percentage on the flutter behaviors of the beams.

Keywords: Functionally graded materials; Aeroelastic flutter; Ritz method; Hydrogen functionalization

1. INTRODUCTION

It is crucial to study the aeroelastic flutter behaviors of structures under supersonic airflow due to the rapid development of technology and the increasing speed of aviation structures [1,2]. Extensive attentions have been attracted on composite structures under supersonic airflow, for the examination of the effects of parameters of components on the flutter behaviors based on analytic, numerical, and experimental methods [3-5]. In the past decades, carbon-based nanocomposite materials are widely used in aerospace, shipbuilding, automobile, and other engineering fields because of their excellent mechanical properties [6-8]. As one of new emerging nanocomposites, graphene platelet (GPL)-reinforced nanocomposites (GPLRCs) have good application prospect in aerospace fields since GPLs have better enhancement effect, compared with other carbon-based reinforcements [9]. Reasonably distributed GPLs can greatly improve the mechanical properties of the composites and meet the needs of the aerospace industry [10,11]. Song et al. [12,13] analyzed the vibrational, buckling and post-buckling behaviors of functionally graded (FG)-GPLRC plates, and proved that, adding a small amount of GPLs can greatly increase the natural frequencies of the plates and reduce the dynamic deflections. Kiani et al. [14] studied the buckling behaviors of FG-GPLRC structures in thermal environment.

Recent investigations show that the presence of functional groups on the surface of graphene can make it more easily dispersed in the matrix and improve the mechanical performance of the composites [15]. Hwang et al. [16] showed that the addition of functional groups helps to prepare graphene/copper nanocomposites with uniformly dispersed graphene, which can significantly improve the mechanical properties of the matrix materials. Zhao et al. [17] found that adding functional groups to graphene/copper-based nanocomposites can greatly improve the interfacial shear strength between

the components.

Halpin-Tsai model [18,19] is an empirical model that is used to predict the elastic properties of nanocomposite materials. Yang et al. [11] proposed a modified Halpin-Tsai model, which has been widely used in prediction of Young's modulus of GPL-reinforced composites due to its high accuracy. However, the traditional models don't consider the effects of, such as functionalization and defects of graphene nanoplatelets. Zhao et al. [20] furtherly modified the micromechanics models based on machine learning (ML) assistance to consider the effects of temperature change and hydrogen functionalization on GPLs. Based on these modified models, they studied the buckling behavior of FG hydrogen-functionalized graphene nanoplatelets (HFGRC) beams. Their results showed that GPLs with hydrogen functionalization have a better reinforcement for the beams. Till now, structural analysis of HFGRC structures is very limited. To the authors' best knowledge, aeroelastic flutter of this new type of nanocomposite structures hasn't been reported yet in the previous studies.

This paper deals with the aeroelastic problem of the FG-HFGRC beams under supersonic airflow. Based on the ML-modified Halpin-Tsai model, the temperature-dependent material properties are evaluated. Governing equations of motions of the beams are established based on the first-order shear deformation theory (FSDT), and the aerodynamic pressure is evaluated by the piston theory. The dynamic equations are spatially discretized by using the Hamilton's principle combined with Ritz trial functions. Flutter velocities are obtained by numerically solving the eigenvalue equation. After a convergence study and a validation study to verify the present approach, a parametric analysis is carried out to examine the effects of boundary conditions, GPL distribution pattern, temperature change, and hydrogenation percentage on the aeroelastic flutter velocities of the beams.

2. FORMULA DERIVATION

A GPLs/copper nanocomposite beam with *N* perfectly bonded layers is shown in Fig. 1. GPLs are hydrogen-functionalized and are randomly oriented and uniformly dispersed in the copper matrix within each layer, whose concentration changes layer by layer along the thickness direction to form a functionally graded structure. In this work, we consider three GPL distribution patterns:

$$\text{UD:}\quad \Theta_G^{(k)} = 1 \tag{1a}$$

$$\text{FG-O:}\quad \Theta_G^{(k)} = 2\left(1-\left|2k-N_{\mathrm{L}}-1\right|/N_{\mathrm{L}}\right) \tag{1b}$$

$$\text{FG-X:}\quad \Theta_G^{(k)} = 2\left|2k-N_{\mathrm{L}}-1\right|/N_{\mathrm{L}} \tag{1c}$$

in which $V_G^{(k)} = V_G\Theta_G^{(k)}$ is the volume fraction of GPLs in the *k*th layer.

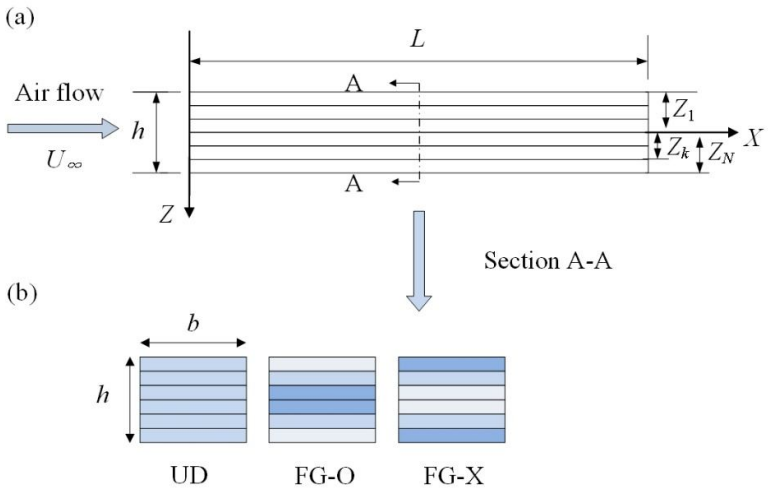

Fig. 1 (a) An FG-HFGRC nanocomposite beam under the supersonic airflow; (b) three GPL distribution patterns

2.1 Material Properties

In this paper, square GPLs with average length l_{G}, and thickness h_{G} are considered. According to the ML-modified Halpin-Tsai model [16], Young's modulus $E_{\mathrm{C}}^{(k)}$ of the *k*th layer are calculated by

$$E_{\mathrm{C}}^{(k)}=\frac{1+2\xi\eta V_{\mathrm{G}}^{(k)}}{1-\eta V_{\mathrm{G}}^{(k)}}\times E_{\mathrm{M}}\times f_{E}\left(F_{G},V_{G},T\right) \tag{2}$$

where the subscripts 'G' and 'M' represent GPL and matrix, respectively; $\xi=l_{\mathrm{G}}/h_{\mathrm{G}}$ is the GPL length-to-thickness ratio, and

$$\eta=\frac{\left(E_{\mathrm{G}}/E_{\mathrm{M}}\right)-1}{\left(E_{\mathrm{G}}/E_{\mathrm{M}}\right)+2\xi} \tag{3}$$

Based on the ML-modified mixing rule, Poisson's ratio $\nu_{\mathrm{C}}^{(k)}$, mass density $\rho_{\mathrm{C}}^{(k)}$, and thermal expansion coefficient $\alpha_{\mathrm{C}}^{(k)}$ can be calculated by

$$\nu_{\mathrm{C}}^{(k)}=\left[\nu_{\mathrm{G}}V_{\mathrm{G}}^{(k)}+\nu_{\mathrm{M}}\left(1-V_{\mathrm{G}}^{(k)}\right)\right]\times f_{\nu}\left(F_{G},V_{G},T\right) \tag{4a}$$

$$\rho_{\mathrm{C}}^{(k)}=\left[\rho_{\mathrm{G}}V_{\mathrm{G}}^{(k)}+\rho_{\mathrm{M}}\left(1-V_{\mathrm{G}}^{(k)}\right)\right]\times f_{\rho}\left(F_{G},V_{G},T\right) \tag{4b}$$

$$\alpha_{\mathrm{C}}^{(k)}=\left[\alpha_{\mathrm{G}}V_{\mathrm{G}}^{(k)}+\alpha_{\mathrm{M}}\left(1-V_{\mathrm{G}}^{(k)}\right)\right]\times f_{\alpha}\left(F_{G},V_{G},T\right) \tag{4c}$$

respectively. The modification functions in Eq. (4) are

$$f_E(F_G,V_G,T)=1.11-1.45V_G-0.132\left(\frac{T}{T_0}\right)+3.18V_G^2-5.96F_GV_G+0.571V_G\left(\frac{T}{T_0}\right) \quad (5a)$$

$$f_v(F_G,V_G,T)=0.827+19.2V_G+0.15\left(\frac{T}{T_0}\right)-285V_G^2+1044V_G^3+47.1F_GV_G-1500F_G^2V_G^2 \quad (5b)$$

$$f_\rho(F_G,V_G,T)=1.01+0.095V_G-1.31V_G^2-0.0144\left(\frac{T}{T_0}\right)-4.45F_GV_G \quad (5c)$$

$$f_\alpha(F_G,V_G,T)=0.963-0.206V_G+0.0542\left(\frac{T}{T_0}\right)+1.95F_GV_G \quad (5d)$$

where $F_G^{(k)}=F_G\Theta_G^{(k)}$ is the hydrogenation percentage of the *k*th layer. Accordingly, the three distribution patterns of hydrogen functionalization are called as UD, F_G-O, and F_G-X, respectively.

2.2 Governing Equations

The coordinate system is established, and its origin is located at point *O*. According to the FSDT, the longitudinal and transverse displacements of the beam are

$$\bar{U}(X,Z,t)=U(X,t)+Z\psi(X,t),\quad \bar{W}(X,Z,t)=W(X,t) \quad (6)$$

in which $U(X,t)$ and $W(X,t)$ are the displacements of a point at the midplane; $\psi(X,t)$ is the rotating displacement; *t* is time. The relationships of strain-displacement are

$$\varepsilon_{xx}=\frac{\partial U}{\partial X}+Z\frac{\partial \psi}{\partial X},\quad \gamma_{xz}=\frac{\partial W}{\partial X}+\psi \quad (7)$$

The relationships of the stress and strain are

$$\sigma_{xx}^{(k)}=Q_{11}^{(k)}\left[\frac{\partial U}{\partial X}+Z\frac{\partial \psi}{\partial X}\right],\quad \sigma_{xz}^{(k)}=Q_{55}^{(k)}\left(\frac{\partial W}{\partial X}+\psi\right) \quad (8)$$

$$\sigma_{xx}^{T(k)}=-Q_{11}^{(k)}\alpha_{\mathrm{C}}^{(k)}\Delta T \quad (9)$$

Where

$$Q_{11}^{(k)}=\frac{E_{\mathrm{C}}^{(k)}}{1-\nu_{\mathrm{C}}^{(k)2}},\quad Q_{55}^{(k)}=\frac{1}{2}\frac{E_{\mathrm{C}}^{(k)}}{1+\nu_{\mathrm{C}}^{(k)}} \quad (10)$$

ΔT is the temperature change. Through Eqs. (6)-(10), the kinetic energy *T* and strain energy *V* can be expressed as

$$T=\frac{1}{2}\sum_{k=1}^{N_L}\int_0^L\int_{Z_k}^{Z_{k+1}}\rho_{\mathrm{C}}^{(k)}\left[\left(\frac{\partial U}{\partial t}+Z\frac{\partial \psi}{\partial t}\right)^2+\left(\frac{\partial W}{\partial t}\right)^2\right]\mathrm{d}Z\mathrm{d}X \tag{11a}$$

$$V=\frac{1}{2}\sum_{k=1}^{N_L}\int_0^L\int_{Z_k}^{Z_{k+1}}\left\{Q_{11}^{(k)}\left[\frac{\partial U}{\partial X}+Z\frac{\partial \psi}{\partial X}\right]^2+Q_{55}^{(k)}\left(\frac{\partial W}{\partial X}+\psi\right)^2\right\}\mathrm{d}Z\mathrm{d}X \tag{11b}$$

The stiffness and inertia related terms and the thermal stress resultant are

$$\left\{I_1,I_2,I_3\right\}=\sum_{k=1}^{N_L}\int_{Z_k}^{Z_{k+1}}\rho_C^{(k)}\left\{1,Z,Z^2\right\}\mathrm{d}Z \tag{12a}$$

$$\left\{A_{11},B_{11},D_{11}\right\}=\sum_{k=1}^{N_L}\int_{Z_k}^{Z_{k+1}}Q_{11}^{(k)}\left\{1,Z,Z^2\right\}\mathrm{d}Z \tag{12b}$$

$$A_{55}=\sum_{k=1}^{N_L}\int_{Z_k}^{Z_{k+1}}\kappa Q_{55}^{(k)}\mathrm{d}Z \tag{12c}$$

$$\alpha_{11}=\sum_{k=1}^{N_L}\int_{Z_k}^{Z_{k+1}}\alpha_{\mathrm{C}}^{(k)}\mathrm{d}Z \tag{12d}$$

where the shear correction factor is $\kappa=5/6$. The strain energy owing to thermal stress and the work done by the aerodynamic pressure can be expressed as

$$V_T=\sum_{k=1}^{N_L}\int_{Z_k}^{Z_{k+1}}\int_0^L\left(-Q_{11}^{(k)}\alpha_{11}\Delta T\frac{\partial W}{\partial X}\delta\frac{\partial W}{\partial X}\right)\mathrm{d}Z\mathrm{d}X \tag{13a}$$

$$\delta\Upsilon_P=\int_0^L\Delta p\delta W\mathrm{d}X \tag{13b}$$

In Eq. (13a), the aerodynamic pressure acting on the beam can be evaluated by the piston theory

$$\Delta p=-\xi\frac{\partial W}{\partial X}-\mu\frac{\partial W}{\partial t} \tag{14}$$

Where

$$\xi=\frac{\rho_\infty U_\infty^2}{\sqrt{M_\infty^2-1}},\ \mu=\frac{\rho_\infty U_\infty}{\sqrt{M_\infty^2-1}}\frac{M_\infty^2-2}{M_\infty^2-1} \tag{15}$$

in which ρ_∞, U_∞ and M_∞ denote the flow density, flow velocity, and Mach number, respectively. Note that the damping term in Eq. (14) is ignoring in the following analysis since it has little influence on the critical flutter velocity.

3. SOLITION PROCEDURE

Based on the following dimensionless quantities

$$x=\frac{X}{L},\ (u,w)=\frac{(U,W)}{h},\ \varphi=\psi,\ \eta=\frac{L}{h},\ \left(\bar{I}_1,\bar{I}_2,\bar{I}_3\right)=\frac{1}{I_{1\mathrm{M}}}\left(I_1,\frac{I_2}{h},\frac{I_3}{h^2}\right),$$
$$\left(a_{11},a_{55},b_{11},d_{11}\right)=\frac{1}{A_{11\mathrm{M}}}\left(A_{11},A_{55},\frac{B_{11}}{h},\frac{D_{11}}{h^2}\right),\ \beta=\frac{\xi L}{A_{11\mathrm{M}}},\ \delta=\frac{\mu L}{\sqrt{A_{11\mathrm{M}}I_{1\mathrm{M}}}},\tau=\frac{t}{L}\sqrt{\frac{A_{11\mathrm{M}}}{I_{1\mathrm{M}}}} \tag{16}$$

Eqs. (11a)-(11b) and (13a)-(13b) can be expressed in dimensionless form as follows

$$T^*=\frac{1}{2}\int_0^l\left[\bar{I}_1\left(\frac{\partial u}{\partial\tau}\right)^2+2\bar{I}_2\frac{\partial u}{\partial\tau}\frac{\partial\varphi}{\partial\tau}+\bar{I}_3\left(\frac{\partial\varphi}{\partial\tau}\right)^2+\bar{I}_1\left(\frac{\partial w}{\partial\tau}\right)^2\right]\mathrm{d}x \tag{17a}$$

$$V^*=\frac{1}{2}\int_0^l\left[a_{11}\left(\frac{\partial u}{\partial x}\right)^2+2b_{11}\frac{\partial u}{\partial x}\frac{\partial\varphi}{\partial x}+d_{11}\left(\frac{\partial\varphi}{\partial x}\right)^2+a_{55}\left(\frac{\partial w}{\partial x}+\eta\varphi\right)^2\right]\mathrm{d}x \tag{17b}$$

$$V_T^*=\int_0^l\left[-a_{11}\alpha_{11}\Delta T\left(\frac{\partial w}{\partial x}\right)^2\right]\mathrm{d}x \tag{17c}$$

$$\Upsilon_P^*=\int_0^l\left(-\beta\frac{\partial w}{\partial x}w-\delta\frac{\partial w}{\partial\tau}w\right)\mathrm{d}x \tag{17d}$$

where $\left\{T^*,V^*,V_T^*,\Upsilon_{\mathrm{p}}^*\right\}=\frac{L}{A_{11\mathrm{M}}h^2}\left\{T,V,V_T,\Upsilon_{\mathrm{p}}\right\}$, $\Delta p^*=\frac{L^2}{A_{11\mathrm{M}}h}\Delta p$.

The Ritz method is used to establish the spatially discretized dynamic equations. The displacements $u(x,\tau)$, $w(x,\tau)$ and $\varphi(x,\tau)$ are expressed as

$$u=\sum_{j=1}^{N}R_{1j}\Psi_{1j} \tag{18a}$$

$$w=\sum_{j=1}^{N}R_{2j}\Psi_{2j} \tag{18b}$$

$$\varphi=\sum_{j=1}^{N}R_{3j}\Psi_{3j} \tag{18c}$$

The trial function Ψ_{1j}, Ψ_{2j} and Ψ_{3j} are used to meet the clamped-clamped (C-C), the clamped-hinged (C-H), the clamped-free (C-F) boundary conditions:

$$\text{the C-C beam: } \Psi_{1j}=\Psi_{2j}=\Psi_{3j}=x^j(1-x) \tag{19a}$$

the C-H beam: $\Psi_{1j} = \Psi_{2j} = x^j(1-x),\ \Psi_{3j} = x^j,$ (19b)

the C-F beam: $\Psi_{1j} = \Psi_{2j} = \Psi_{3j} = x^j$ (19c)

Based on Hamilton's principle

$$\delta\int_{\tau_0}^{\tau_1}\left(T^* - V^* - V_T^*\right)\mathrm{d}\tau + \int_{\tau_0}^{\tau_1}\delta\Upsilon_P^*\mathrm{d}\tau = 0 \tag{20}$$

the ordinary differential equation in matrix form is obtained:

$$\mathbf{M}\ddot{\mathbf{d}} + \left(\mathbf{K} + \beta\mathbf{K}_{\Delta P} - \Delta T\mathbf{K}_{\Delta T}\right)\mathbf{d} = \mathbf{0} \tag{21}$$

where $\mathbf{d} = \left\{\mathbf{R}_1^T\ \mathbf{R}_2^T\ \mathbf{R}_3^T\ \right\}^T$, and $\mathbf{R}_r = [R_{r1}\quad R_{r2}\quad \cdots\quad R_{rN}]$.

The general solution of Eq. (21) can be expressed as

$$\mathbf{d} = \mathbf{d}_0 e^{\lambda t} \tag{22}$$

where $\mathbf{d}_0$ and λ are the eigenvector and eigenvalue, respectively. By substituting Eq. (22) into Eq. (21), the eigenvalue problem is established in matrix form:

$$\left[\mathbf{M}\lambda^2 + \left(\mathbf{K} + \beta\mathbf{K}_{\Delta P} - \Delta T\mathbf{K}_{\Delta T}\right)\right]\mathbf{d}_0 = 0 \tag{23}$$

where $\mathbf{M}$ is the mass matrix, $\mathbf{K}$ is the stiffness matrix, $\mathbf{K}_{\Delta P}$ and $\mathbf{K}_{\Delta T}$ are matrices related to the aerodynamic force and the thermal effect, respectively. To get a non-trivial solution of Eq. (23), its coefficient determinant should be zero:

$$\left|\mathbf{M}\lambda^2 + \left(\mathbf{K} + \beta\mathbf{K}_{\Delta P} - \Delta T\mathbf{K}_{\Delta T}\right)\right| = 0 \tag{24}$$

After solving Eq. (24), the *i*th natural frequency can then be obtained by

$$\omega_i = \sqrt{\left[\mathrm{Im}\left(\lambda_i\right)\right]^2},\ i = 1, 2, ..., n. \tag{25}$$

4. NUMERICAL RESULTS AND DISCUSSION

In this section, FG multilayer GPLs/copper beams with 10 layers and a slenderness ratio of 30 are considered. In the following study, unless otherwise stated, the average size of the nanofillers is 2.5μm×2.5μm×1.5nm, and the total GPL weight fraction is 0.6%. The material parameters can be found in [16].

4.1 Comparison Studies

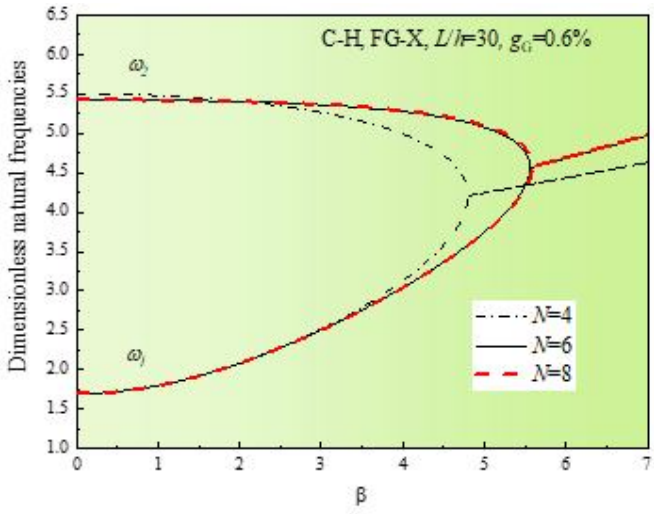

Fig. 2 Natural frequencies of the supersonic FG-HFGRC beams with different truncation terms.

Fig. 2 shows the dimensionless natural frequencies of FG-HFGRC beams with different polynomial terms *N*, taking the FG-X beam with C-H boundary conditions as an example. Convergent solutions can be obtained when the number of truncation terms is increased to 6. In this case, *N* = 6 is used for the subsequent calculations. To verify the effectiveness of the present method, the present results are compared with those in Ref. [4]. Note that the parameters in this validation study are: Young's modulus, Poisson's ratio and density are 70 GPa, 0.3, and 2710 kg·m^{-3}, respectively, and the length, width and thickness of the beam are 0.3m, 0.03m and 0.004m, respectively. It can be seen from Table 1, the present results are consistent with the results in Ref. [4], which proves the effectiveness of the present method.

Table 1 The first two natural frequencies of a supersonic beam with C-F boundary conditions

$\bar{\beta}$		Ω_1	Ω_2
4	Ref. [4]	760	1639
	Present	760	1562
8	Ref. [4]	1094	1716
	Present	1096	1638
12	Ref. [4]	1564	1564
	Present	1571	1571
16	Ref. [4]	1780	1780

	Present	1760	1760

4.2 Parametric Studies

Fig. 3 analyzes the effect of GPL distribution on the natural frequencies of the FG-HFGRC beams under supersonic airflow. As shown in this figure, with the increase of aerodynamic pressure, the first natural frequencies increase while the second natural frequencies decrease until they merge at the critical points, which means the flutter occurs. Furthermore, it can be observed, among the UD, FG-O and FG-X beams, the FG-X beam has the highest critical flutter velocity, and the FG-O beam has the lowest one.

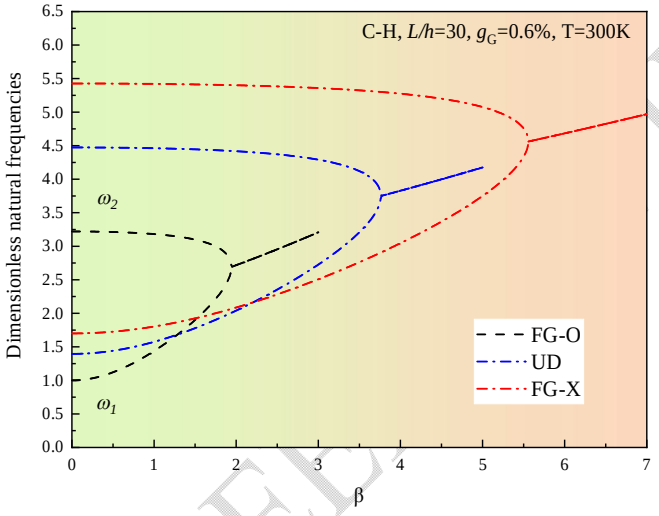

Fig. 3 Effect of GPL distribution pattern on the natural frequencies of supersonic FG-HFGRC beams.

Fig. 4 demonstrates the effect of hydrogenation percentage on the first two natural frequencies of FG-HFGRC beams with different GPL distribution patterns. The hydrogenation percentages are selected as 0, 3 % and 5 %, respectively. A fact demonstrated in Ref. [20] should be noted, i.e., a higher degree of hydrogen functionalization results a combining effect, i.e., a larger Poisson's ratio and a lower Young's modulus. It can be seen from Fig. 4 that the critical flutter velocity increases with the hydrogenation percentage, demonstrating that a combining effect caused by the increase of hydrogenation percentage can enhance the beam. This is consistent with the observation in the buckling analysis of the FG-HFGRC beams in Ref. [20].

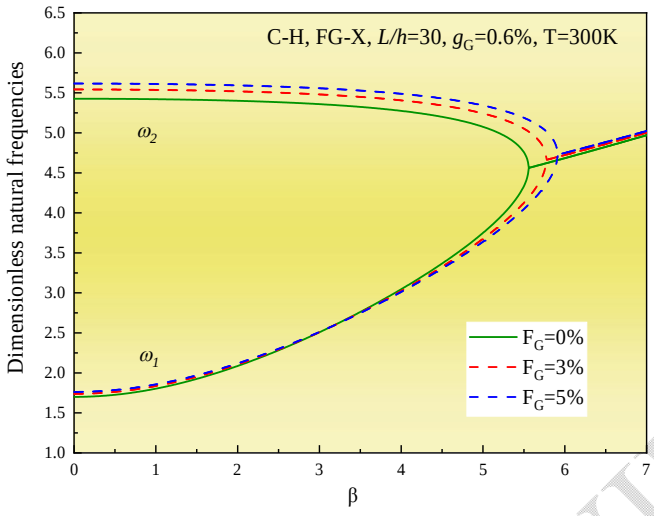

Fig. 4 Effect of hydrogenation percentage on the natural frequencies of supersonic FG-X beams.

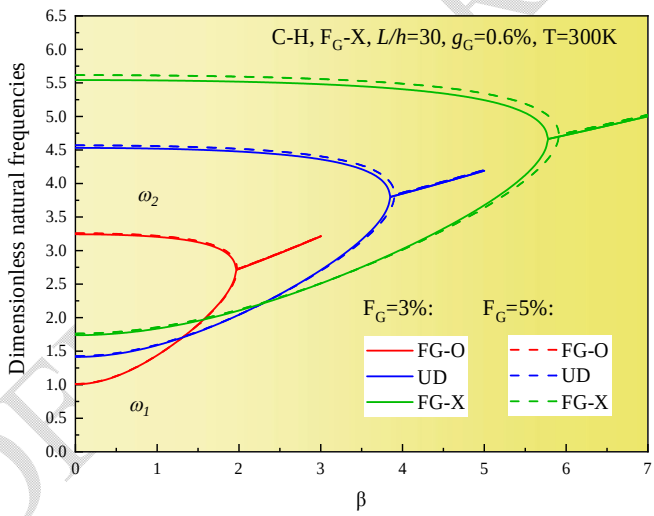

Fig. 5 Effect of hydrogenation percentage on the natural frequencies of supersonic FG-HFGRC beams with different GPL distribution patterns.

Fig. 5 displays the effect of hydrogenation percentage on the first two dimensionless natural frequencies of the supersonic FG-HFGRC beams with different GPL distribution patterns. As can be observed, the hydrogenation percentage has the greatest influence on the critical flutter velocity of the FG-X beam and has the least influence on the FG-O beam. Fig. 6 demonstrates the effect of distribution pattern of the hydrogen functionalization on the natural frequencies of the UD beam. Note that the GPL concentration in the whole beam is a constant; the functionally graded material properties are formed by different layer-wise variations of degree of hydrogen functionalization. As can be seen, bonding more hydrogen functional groups on the surfaces of GPLs farther away from the midplane of the beam can result a larger critical flutter velocity.

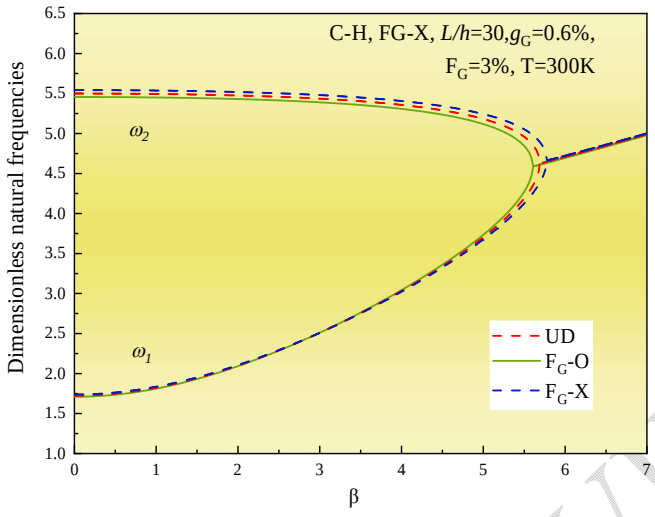

Fig. 6 Effect of distribution pattern of hydrogen functionalization on the natural frequencies of supersonic FG-HFGRC beams.

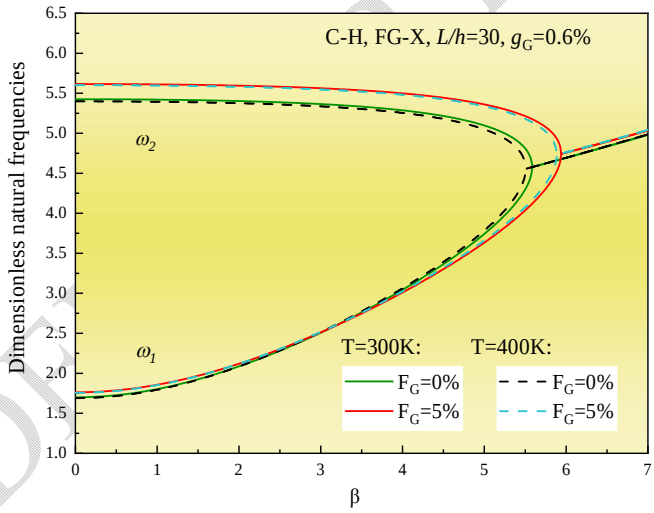

Fig. 7 Effect of temperature change on the natural frequencies of supersonic FG-HFGRC beams.

Due to the friction between the beam and the supersonic airflow, temperature of the beam will rise. Fig. 7 investigates the effect of temperature change on the dimensionless natural frequencies of supersonic FG-HFGRC beams, taking the C-H boundary conditions as an example. For the calculation, the initial temperature is set to be 300K. Two cases when the hydrogenation percentage is selected to be 0% and 5% are considered. As can be seen that, the critical flutter velocity of the beam considerably decreases as the temperature rises from 300K to 400K. This is because the temperature rise reduces the bending stiffness of the C-H beam. This observation is helpful to remind the engineers to take the temperature factors into account during the material and structural design process for FG-HFGRC aviation structures.

5. CONCLUSIONS

This paper studies the aeroelastic flutter characteristics of FG-GPLRC beams, considering the hydrogen functionalization on the surfaces of GPLs. The material properties of the FHGRC are evaluated by the ML-assisted Halpin-Tsai model and mixture rule. The formula derivation for the motions of the beams is within the framework of the FSDT, and the solution method is based on the Hamilton's principle together with Ritz trial functions. The main conclusions are: (1) Adding hydrogen functional groups on the surfaces of the GPLs can improve the critical flutter velocities of the beams, and the greater the degree of hydrogen functionalization, the higher the critical flutter velocities. (2) Adding more hydrogen functional groups far away the midplane of the beams is an effective way to furtherly improve the critical flutter velocities. (3) The temperature rise considerably reduces the critical flutter velocities of the FG-FHGRC beams.

REFERENCES

[1] Nathan H. Applied aerodynamics. Aerospace America. 2012; 50(11):15.

[2] Wolfgang M, Karsten S. Aerodynamics and Aeroacoustics. A TZextra worldwide. 2010; 15(11):74-81.

[3] Li FM, Song ZG. Aeroelastic flutter analysis for 2D Kirchhoff and Mindlin panels with different boundary conditions in supersonic airflow. Acta Mechanica.2014; 225:3339-3351.

[4] Zhou K, Ni Z, Hua H, Nonlinear aero-thermo-elastic characteristics analysis of porous FGM beams with general boundary conditions. Journal of Vibration and Shock. 2021; 40(20):34-41.

[5] Kouchakzadeh MA, Rasekh M, Haddadpour H. Panel flutter analysis of general laminated composite plates. Composite Structures. 2010; 92:2906-2915.

[6] Potts JR, Dreyer DR, Bielawski CW, Ruoff RS. Graphene-based polymer nano-composites. Polymer. 2011; 52:5-25.

[7] Kuilla T, Bhadra S, Yao D, Kim NH, Bose S, Lee JH. Recent advances in graphene-based polymer composites. Progress in Polymer Science. 2010; 35:1350-75.

[8] Huang X, Qi X, Boey F, Zhang H. Graphene-based composites. Chemical Society Reviews. 2012; 41:666-86.

[9] Rafiee MA, Rafiee J, Wang Z, Song HH, Yu ZZ, Koratkar N. Enhanced mechanical properties of nanocomposites at low graphene content[J]. ACS nano. 2009;3(12):3884-90.

[10] Zhao SY, Zhao Z, Yang ZC, Ke LL, Kitipornchai S, Yang J. Functionally graded graphene reinforced composite structures: A review[J]. Engineering Structures. 2020; 210(C):110339.

[11] Yang J, Wu HL, Kitipornchai S. Buckling and postbuckling of functionally graded multilayer graphene platelet-reinforced composite beams[J]. Composite Structures. 2017; 161:111-118.

[12] Song MT, Kitipornchai S, Yang J. Free and forced vibrations of functionally graded polymer composite plates reinforced with graphene nanoplatelets. Composite Structures. 2017; 159:579-588.

[13] Song MT, Yang J, Kitipornchai S. Bending and buckling analyses of functionally graded polymer

composite plates reinforced with graphene nanoplatelets. Composites Part B: Engineering. 2018; 134:106-113.

[14] Kiani Y. Buckling of functionally graded graphene reinforced conical shells under external pressure in thermal environment. Composites Part B: Engineering.2018; 156:128-37.

[15] Ian A. Kinloch, Jonghwan Suhr, Jun Lou, Robert J. Young, Pulickel M. Ajayan. Composites with carbon nanotubes and graphene: An outlook[J]. Science. 2018; 362(6414):547-553.

[16] Hwang J, Yoon T, Jin S H, et al. Enhanced mechanical properties of graphene/copper nanocomposites using a molecular-level mixing process[J]. Advanced materials (Deerfield Beach, Fla.),2013; 25(46):6724-6729.

[17] Zhao S Y, Zhang Y Y, Yang J, Kitipornchai S. Significantly improved interfacial shear strength in graphene/copper nanocomposite via wrinkles and functionalization: A molecular dynamics study[J]. 2021,174:335-344.

[18] Peter Wall. A Comparison of homogenization, Hashin-Shtrikman bounds and the Halpin-Tsai Equations[J]. Applications of Mathematics. 1997; 42(4):245-257.

[19] Halpin JC, Kardos JL. The Halpin-Tsai equations: a review. Polymer Engineering Science. 1976; 16:344-52.

[20] Zhao SY, Zhang YY, Zhang YH, Zhang W, Yang J, Kitipornchai S. Buckling of functionally graded hydrogen-functionalized graphene reinforced beams based on machine learning-assisted micromechanics models[J]. European Journal of Mechanics / A Solids. 2022; 96:14675.